A 5-DOFs Robot for Posterior Segment Eye Microsurgery

Ning Wang[1,4], *Student Member, IEEE,* Xiaodong Zhang[2], *Member, IEEE*, Mingyang Li[2], Hongbing Zhang[3], Danail Stoyanov[4], *Senior Member, IEEE,* Agostino Stilli[4], *Member, IEEE*

***Abstract* – In retinal surgery clinicians access the internal volume of the eyeball through small scale trocar ports, typically 0.65 mm in diameter, to treat vitreoretinal disorders like idiopathic epiretinal membrane and age-related macular holes. The treatment of these conditions involves the removal of thin layers of diseased tissue, namely the epiretinal membrane and the internal limiting membrane. These membranes have an average thickness of only 60 µm and 2 µm respectively making extremely challenging even for expert clinicians to peel without damaging the surrounding tissue.**

In this work we present a novel Ophthalmic microsurgery Robot (OmSR) designed to operate a standard surgical forceps used in these procedures with micrometric precision, overcoming the limitations of current robotic systems associated with the offsetting of the remote centre of motion of the end effector when accessing the sclera. The design of the proposed system is presented, and its performance evaluated.

The results show that the end effector can be controlled with an accuracy of less than 30 µm and the surgical forceps opening and closing positional error is less than 4.3 µm. Trajectory-following experiments and membrane peeling experiments are also presented, showing promising results in both scenarios.

Index Terms – Mechanism Design, Medical Robots and Systems

I. Introduction

The 2019 World Health Organization survey on eye diseases showed that more than 2 billion people in the world are suffering from some form of vision impairment with almost 200 million people suffering of age-related macular degeneration [1]. Other common retinal disorders include idiopathic epiretinal membrane, diabetic retinopathy, retinal detachment, and retinal vein occlusion. All these conditions are associated with the posterior segment of the eye, the accessibility of which is strongly limited by the small workspace inside the vitreous humour [2]. Typically, in retinal microsurgery, with the aid of a microscope, long, thin ophthalmic tools are inserted through the sclera to access the internal volume of the eyeball to perform delicate surgical tasks in the posterior segment of the eye [3]. Although this type of surgery is widely performed to treat fundus diseases, these procedures are still challenging for clinicians due to multiple factors. The first is that the intraocular surgical volume is small, being the average diameter of the eyeball of an adult human 22 mm with its volume being on average only around 6 cm^3 [4]. The second factor is the visibility which is typically very low inside the vitreous humour; thus, it is challenging for clinicians to judge the distance between the Internal Limiting Membrane (ILM), the tools and the retina. This problem is particularly prominent in ILM and Epiretinal Membrane (ERM) surgery [5], a procedure where the clinician peels off this membrane from the surface of the retina typically to treat age-related macular holes. The ILM is almost transparent and less than 20 µm thin; even when biocompatible stain is applied on it to enhance contrast and a high-magnification microscope is used to observe it, even expert clinicians can struggle to detect it. To overcome the limitations associated with the low visibility of the surgical scene and the minimal thickness of the ILM clinicians mostly rely on experience to judge its position. Furthermore, using surgical forceps they poke the fundus tissue to make it locally deform to reflect light differently from the background to gain information about the depth of the scene.

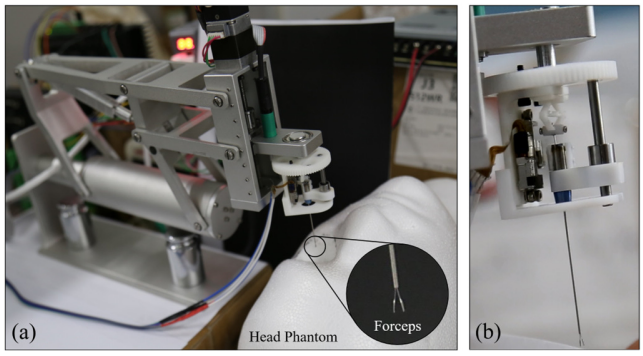

Figure 1 - Overview of the OmSR robot (a) and close-up of forceps (circle) and close-up of the EE (b).

The second problem that follows is that the doctor's arm has an inherent natural subtle jitter the magnitude of which is around 100 µm [6], which will drive the surgical forceps to vibrate at a frequency of 10 Hz, posing a concrete risk of damaging the fundus tissue. The third one is that the interaction force between surgical instruments and fundus tissue during fundus surgery is very small, less than 10 mN [7]. The sensory feedback from these hand-held micro tools is so minimal that typically the clinician cannot properly perceive such a small interaction force, hence, this can only be estimated using visual feedback and experience, which reduces the accuracy of the operation.

These challenging procedures frequently require repeated attempts over an extended period of time to succeed [8]. Unsuccessful peeling can result in poor visual outcome [9]. The study presented in [10] showed that up to 50% of the

Manuscript received: February 24, Year; Revised: June 2, 2022; Accepted: June 23, 2022.

This paper was recommended for publication by Editor Jessica Burgner-Kahrs upon evaluation of the Associate Editor and Reviewers' comments.

[1]Ning Wang is with the School of Mechanical Eng., Xi'an Jiaotong University, Xi'an 710049 China. (email: JL21701204@mail.xjtu.edu.cn)

[2]Xiaodong Zhang and Mingyang Li are with the School of Mechanical Engineering, Xi'an Jiao tong University, Xi'an 710049, China. (e-mail: xdzhang@mail.xjtu.edu.cn, mingyangli0825@163.com)

[3]Hongbing Zhang is with No.1 Xi'an Hospital, Xi'an 710002, China. (e-mail: zhanghongbing01@163.com)

[4]Ning Wang, Danail Stoyanov and Agostino Stilli are with the Wellcome/EPSRC Centre for Interventional and Surgical Sciences, University College London, London WC1E 6BT UK. (e-mail: w.ning@ucl.ac.uk, danail.stoyanov@ucl.ac.uk, a.stilli@ucl.ac.uk).

Digital Object Identifier (DOI): see top of this page.

patients exhibited micro injuries in the layer around the macula after peeling. Therefore, to meet these clinical challenges and improve the success rate of these procedures researchers have started to investigate the use of robotic systems for eye surgery [11].

Robotic assistance in eye surgery was first investigated in the 1980s [12]. In the recent work of Jingjing et al. [3] and Morris et al. [11], [13], the history of robotic-assisted eye surgery is widely discussed and a structural classification of the most important research and commercial ophthalmic surgical robots is presented. Handheld surgical robots such as the Micron [14] have been proposed, but over the years the research community has been driven more and more towards more master-slave closed-chain designs. Researchers have also investigated alternative designs like those presented in [15] and [16], yet the limited workspace of the End Effector (EE) of these systems hindered their clinical translation.

The other main design topology investigate by the research community has been the articulated parallelogram. The main advantage of this mechanism over arc and spherical rails is that it can create a much slenderer design while maintaining better lateral stiffness on the surgical instrument shaft. In this configuration the workspace is a circular sector centred on the eye; this allows free movement of the core robotic structure far from the head of the patient, ensuring accessibility of other hand-held or robotic instruments, illumination devices like the chandelier while leaving the field of view of the microscope unobstructed. Therefore, this design topology has become the most widely researched in recent years. The team of Prof. Robert E. MacLaren at the University of Oxford used the Preceyes Surgical System (Preceyes B.V., Eindhoven, NL), a robotic system based on an articulated parallelogram, to perform the first clinical intraocular robotic surgery [17].

Micro-surgical forceps are always needed to successfully perform ILM or ERM peeling procedures. The forceps need to be at the right angle with the ILM/ERM to create the initial flap required for peeling. The angular position relationship between the opening of the forceps and the membrane targeted should be adjusted in real time to ensure that the forceps can pick up and peel it [2], [18]. This requires not only three DOFs for forceps positioning, but also two DOFs for forceps to spin around the insertion axis and open/close. Nonetheless, to date both in academic and industrial research teams, no one has succeeded in integrating in an articulated parallelogram structure a surgical forceps that can be actively controlled both in terms of opening/closure and 4-DOFs navigation, enabling complex surgical operations through either automatic control or master-slave control, helping clinicians achieve non-invasive surgery.

The main limitation is that most robotic structures, excluding the DOF of movement of the base of the surgical robot, only three or four DOFs are available at the EE and only in a very narrow angle. For example, the ophthalmic surgical robot designed by Gijbels et al. [19]–[21] at Leuven University has only three DOFs and acts only as a stabilizer to hold surgical instruments but cannot actively control the movement such instruments. The Steady-hand Eye Robot (SHER) designed by Taylor et al. [22] has six DOFs, however, two of them are the DOFs of the base frame, and EE has only four degrees of freedom. For this system the orientation accuracy of the EE is about ±1° [23]. The Preceyes ophthalmic surgical robot [17], [24] offers four DOFs at the EE with a position accuracy of the tool tip of 10 μm through a master-slave control. However, it does not provide the extra DOF needed to control instruments that require to control opening and closing motion such as surgical forceps. This limits the use of this system, making it not possible to use it in most vitreoretinal operations where membrane peeling is required.

Lastly, the magnetically guided robot presented in [13] has potential for ERM peeling procedures, nonetheless additional DOFs are needed to successfully perform this task. To date no 5-DOFs ophthalmic robot capable of performing posterior segment eye surgery, including ILM and ERM peeling, has been presented.

In this work, we propose a 5-DOF Ophthalmic microsurgery Robot (OmSR) system. The proposed robot has been designed based on clinical requirements in terms of precision and workspace. The design is optimised to ensure stability of the remote centre of motion (RCM) of the tool. This is achieved embedding a linear push rod motor in a double-parallelogram structure optimising its positioning to achieve the best trade-off between pitching motion transfer efficiency, motion stability and robot motion accuracy. A fibre Bragg grating (FBG) sensor mechanism is also embedded to measure the intraoperative interaction force directly on the EE shaft to potentially enable force feedback for the user.

An overview of the OmSR system is presented in Fig. 1. In section II the design is presented, the forward and inverse kinematics are described, and the design optimisation process explained. Integration of force sensing in the EE is also discussed. In section III motion accuracy of the EE is evaluated as well as the performance of the robot in membrane peeling testing conducted on an eggshell, which closely resemble the thickness of the target membranes in the human eye anatomy. Lastly, in section IV the conclusions and future work are presented.

II. Materials and Methods

A. Improved Double Parallelogram Mechanism Design

A simplified representation of the design iterations investigated for the proposed robotic system is presented in Fig. 2. The simplest approach to the articulated parallelogram design is the integration of two parallelograms as shown in Fig. 2a: the movement of EE on the secondary parallelogram ($\square DEFG$) completely follows the movement of the primary parallelogram ($\square ABCD$). $\square ABCD$ is connected to the world frame through the rod AB, the upper connecting rod CE is shared by two parallelogram mechanisms, and the lower connecting rod FG of $\square DEFG$ is hinged on the left vertical connecting rod AD of $\square ABCD$. In this configuration, when the primary parallelogram mechanism is tilted, the upper rod CE remains horizontal, and the two vertical rods rotate by an angle $(\Psi - \pi/2)$ relative to the vertical direction. If the left connecting rod (EFP) of $\square DEFG$ coincides with the central axis of the EE, the EE will follow (EFG) and rotate by $(\Psi - \pi/2)$ around the point P. If we now rotate the whole structure around the axis passing by AB, the rotation Φ of the EE around point P can be realized, and point P is the RCM of our system.

An improved structure has been proposed by Sajid Nisar [25] and A. Gijbels [20] and is shown in Fig. 2b. The R-direction translation through the relative sliding of the connecting rod AD relative to the joint A is the innovative point of this design. Nonetheless, to add spinning motion

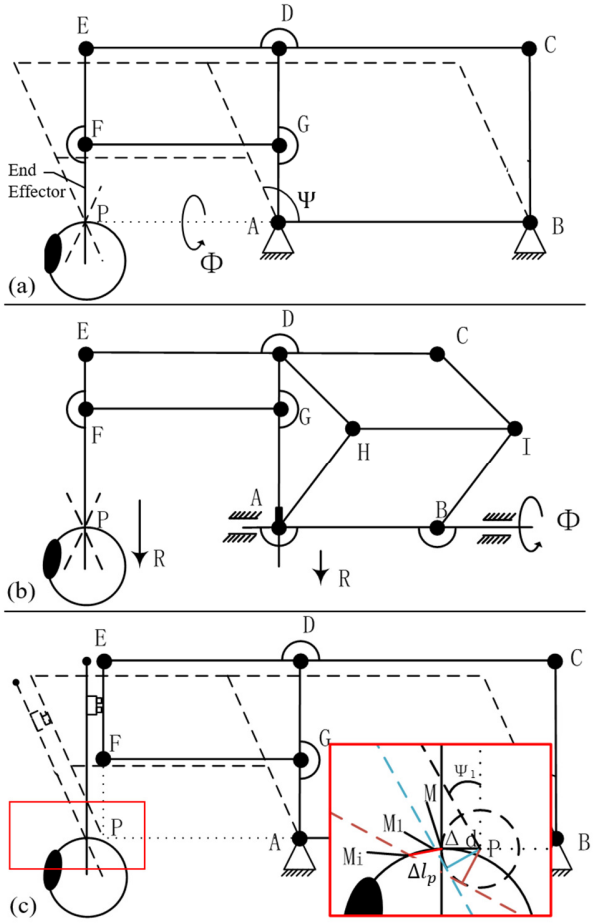

Figure 2 – Design topologies for double articulated parallelogram systems: simple without translation at the EE with fixed RCM (a), advanced with translation at the EE and fixed RCM (b), advanced with translation and rotation at the EE but floating RCM (c).

around FP for the EE an additional actuator is required and the addition of such actuator with this topology would result in the creation of an offset that needs to be compensated. In this design configuration is not trivial to solve this issue.

An approach to overcome this problem would be to use the configuration presented in Fig. 2c where the translation R and the spinning of the EE are enabled by the combination of a linear actuator and a rotational actuator on the EF rod. In this case there will be a Δd offset (see the red box in Fig. 2c) between the EE axis and the straight line where the connecting rod EFP is located. Thus, the insertion point M of the surgical forceps will not coincide with the RCM point P, damaging the sclera where the port is inserted. Point M in this case moves in a circle with point P as the centre and Δd as the radius with the change of Ψ value, resulting in a deviation of Δl_p between the vertical insertion point M and M_i the insertion point at any other angle. The Δl_p can be calculated as:

$$\Delta l_p = MM_i = \frac{\Delta d}{\sin \Psi} - \Delta d \quad (1)$$

Considering this, an improved double articulated parallelogram structure is presented in Fig. 3a. Considering the angle between the line connecting FP and the rod EF as the reference angle, the structures of rod AD and rod BC have been redesigned so that the angle between DG and GA and the angle between CI and IB are the same as the reference angle.

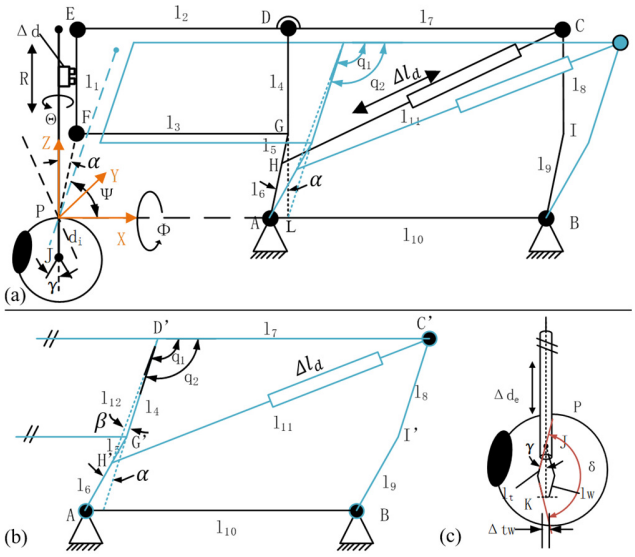

Figure 3 - Schematic of the joint connections in the proposed structure including all the parameters and joint coordinates for all the components of the robotic chain (a) (b) and forceps (c).

In this way we can construct the double articulated parallelogram structure of $\square AGFP$ (virtual parallelogram) and $\square ABCD$.

The angle deviation between DG and GA compensates for the displacement of the EE and ensure that the insertion point M of the surgical forceps coincides with the point P of the RCM, thus ensuring minimal damage to the tissue of the sclera after port insertion. In addition, thanks to this angle the centre of mass of the system will be at a smaller offset from the vertical axis during forward pitch motion when comparing the proposed system with the systems in Fig. 2. Even when the Ψ angle is larger than 90°, most of the weight will be still on the beam AB, ensuring better stability.

To enable this design and to simplify the kinematic chain of the system presented in Fig. 2b a linear push rod motor is integrated between rod AD and rod BC to drive the primary parallelogram mechanism to rotate around joint B, thus driving the pitching motion of the whole robot. This design not only takes advantage of the characteristics of this additional triangular structure to increase stability, but also ensures self-locking of the structure in case of power failure.

B. Design of the Robotic Chain

The final structure is presented in detail in Fig. 3. Each joint of the surgical robot is represented by capital letters. More specifically, the rotating joint are represented by A, B, C, D, E, F, G, H and J purposedly in alphabetical order to highlight the angular relationship between the various rods. Please note that the articulation symbols of G and H joints are not drawn in Fig. 3a to ensure visibility of the other lines, but they are also rotational joints. C', D', G' and H' are the new positions of the corresponding joints under a certain angle of rotation of the mechanism in both Fig. 3a and 3b. The virtual point L is obtained by intersecting the extension of DG with AB, and I is the bending point of the rod BC. The world reference frame XYZ is placed at the EE with the origin in the RCM in point P. As shown in Fig. 3, the proposed design provides a total of five DOFs at the EE, namely: three rotational DOFs (Φ around x-axis, Ψ around y-axis, Θ around

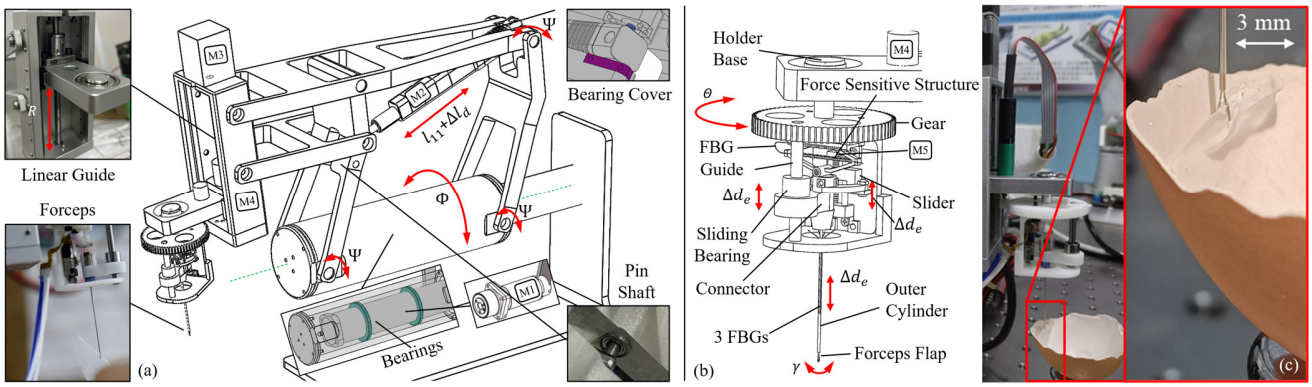

Figure 4 - Overview of the main components of the prototype of the proposed system including the double articulated parallelogram (a) and the effector (b). Motors are labelled from 1 to 5 in the kinematic chain and joint coordinates are indicated as well. On the right the peeling experiment conducted on the internal membrane of an eggshell to simulate the ILM peeling procedure is presented.

z-axis,) one translational DOF (linear motion R along PE), and the opening and closing DOF of the forceps γ Fig. 3 also includes the names of the connecting rods $l_1, l_2 \dots l_{11}$ of the system and the joint angles α, β, q_1, q_2. Here l_5 and l_6 are the distances from joint G to joint H and from joint H to joint A respectively, d_i is the length of the surgical forceps rod extending into the eyeball, l_{11} and $\triangle\, l_d$ are the natural length of the linear push rod motor and the stretching amount of the push rod respectively, α is the design reference angle, which is equal to the angle between the extension line of DG section and GA section on the rod AD and the angle between the extension line of DG section and GA section after the rod AD rotates for a certain angle. β, q_1 and q_2 are the sizes of the angles $\angle H'D'G'$, $\angle H'D'C'$ and $\angle G'D'C'$ respectively.

The parameters introduced have the following relationship: $l_1 = l_4 = l_8$, $l_2 = l_3$, $l_5 + l_6 = l_9$, $l_7 = l_{10}$.

For the EE section, a lead screw mechanism is embedded. The sliding block is attached to the external cylindrical metal case of the surgical forceps of radius r, with the lead screw being driven by a stepper motor. The movement of the slider drives the outer cylindrical metal case causing a Δd_e protrusion of the forceps outside such structure. The opening and closure of the forceps is realized by compressing the two flaps around the joint J at the lower edge of the cylindrical metal case (see Fig. 3c). The two flaps are symmetrical and the distance between the tips of the two is Δtw and the midpoint is K. The lengths of the two segments of the individual flaps are l_t and l_w respectively, and the angle between the two is δ.

C. *Forward Kinematics*

In the Forward Kinematics (FK) we calculate the coordinate (p_x, p_y, p_z) of point K, the most distal point of the EE, as function of the joint variables $(\Phi, \Psi, \Theta, R, \gamma)$.

This, as described by the following formula:

$$(p_x, p_y, p_z) = f_{FK}(\Phi, \Psi, \Theta, R, \gamma) \tag{2}$$

Assuming that the coordinates of point J are (p_x', p_y', p_z'), in the coordinate system XYZ, the displacement from point P in the direction of R is d_i.

Hence, the coordinates of J can be expressed as:

$$\begin{cases} p_x' = -d_i \cos\Psi, \Psi \in [60°, 105°] \\ p_y' = d_i \sin\Phi, \Phi \in [-45°, 45°] \\ p_z' = -d_i \sin\Psi \cos\Phi \end{cases} \tag{3}$$

In the above expression, the DOF Ψ of the robot's pitching motion is provided by the telescopic motion of the linear push rod motor M2 as shown in Fig. 4a. Establishing the functional relationship between the angle Ψ and Δl_d can further describe the corresponding relationship between the end motion of the robot and the driving linear motor. As shown in Fig. 3b, the relative positional relationship of each structure given by the virtual rod l_{12} and the angle β can be obtained as:

$$l_{12} = \sqrt{l_4^2 + l_5^2 + 2l_4 \cdot l_5 \cdot \cos\alpha} \tag{4}$$

$$\beta = sin^{-1}(l_5 \sin\alpha / l_{12}) \tag{5}$$

The relationship between q_1, q_2 and Δl_d is given by:

$$q_1 = cos^{-1}((l_7^2 + l_{12}^2 - (l_{11} + \Delta l_d)^2)/(2l_7 \cdot l_{12})) = \beta + q_2 \tag{6}$$

Therefore, the Ψ and Δl_d functions can be defined as:

$$\Psi = sin^{-1}(l_5 \sin\alpha / l_{12}) + \pi - cos^{-1}((l_7^2 + l_{12}^2 - (l_{11} + \Delta l_d)^2)/(2l_7 \cdot l_{12})) \tag{7}$$

The equation of motion $(p_x', p_y', p_z') = f_{FK}(\Phi, \Psi, \Theta, R)$ can be defined by using (7) into the expression of the coordinates of J as detailed in (3). Thus, the coordinate (p_x, p_y, p_z) of point K can be obtained as follows:

$$\begin{cases} p_x = -[d_i + l_t \cdot \cos\gamma_c - l_w \cdot cos(\delta - \gamma_c)] \cos\Psi \\ p_y = [d_i + l_t \cdot \cos\gamma_c - l_w \cdot cos(\delta - \gamma_c)] \sin\Phi \\ p_z = -[d_i + l_t \cdot \cos\gamma_c - l_w \cdot cos(\delta - \gamma_c)] \sin\Psi \cos\Phi \end{cases} \tag{8}$$

where half of the forceps full opening angle is γ_0 and the close state is γ_c. We can now define the relationship between the rotation angle of the surgical forceps Θ and the position of the EE and at the opening/closing angle of the flaps. The rotation angle Θ of the surgical forceps shall meet the following condition:

$$(\Theta/\Theta_d) = (Z_2/Z_1) \tag{9}$$

Where, Θ_d is the rotation angle of the motor, Z_1 and Z_2 are the number of teeth of the surgical forceps spin gear and the motor spindle gear respectively (see Fig. 4b). The relationship between γ and Δd_e, displacement of outer cylinder of the surgical forceps, can now be derived:

$$\left((r/tan\gamma_0) + \Delta d_e\right) tan\gamma = r \tag{10}$$

$$\gamma = tan^{-1}\left[r/\left((r/tan\gamma_0) + \Delta d_e\right)\right] \tag{11}$$

And the opening size Δtw of the surgical forceps can be expressed as:

$$\Delta tw = l_t(\sin\gamma_0 - \sin\gamma) \tag{12}$$

D. Inverse Kinematics

We can now solve the Inverse Kinematics (IK) of our system, where we want to know the joint coordinates given the position and the opening/closing angle of forceps.

We now want to define the following relationship:

$$(\Phi, \Psi, \Theta, R, \gamma) = f_{IK}(p_x, p_y, p_z) \tag{13}$$

Knowing the position of point K (p_x, p_y, p_z), the variables Φ, Ψ and d_i can calculated as follows:

$$d_i = -l_t\cos\gamma_c + l_w\cos(\delta - \gamma_c) + \frac{\sqrt{2}}{2}\sqrt{{p_x}^2 + {p_y}^2 + {p_z}^2 + \sqrt{{p_x}^4 - 2{p_x}^2{p_y}^2 + 2{p_x}^2{p_z}^2 + {p_y}^4 + 2{p_y}^2{p_z}^2 + {p_z}^4}} \tag{14}$$

$$\Psi = \cos^{-1}\left(-\sqrt{2}p_x \Big/ \sqrt{{p_x}^2 + {p_y}^2 + {p_z}^2 + \sqrt{{p_x}^4 - 2{p_x}^2{p_y}^2 + 2{p_x}^2{p_z}^2 + {p_y}^4 + 2{p_y}^2{p_z}^2 + {p_z}^4}}\right) \tag{15}$$

$$\Phi = \sin^{-1}\left(\sqrt{2}p_y \Big/ \sqrt{{p_x}^2 + {p_y}^2 + {p_z}^2 + \sqrt{{p_x}^4 - 2{p_x}^2{p_y}^2 + 2{p_x}^2{p_z}^2 + {p_y}^4 + 2{p_y}^2{p_z}^2 + {p_z}^4}}\right) \tag{16}$$

Hence, the expression of Θ and Δd_e can be obtained as:

$$\Theta = \Theta_d \cdot (Z_2/Z_1) \tag{17}$$

$$\Delta d_e = (r/tan\gamma) - (r/tan\gamma_0) \tag{18}$$

E. Optimization of Design Parameters

The size data between adult head organs is given in document [26]. The average value of height (chin to top of the head) of an adult head is 184 mm, the average value of the width (ear to ear) of an adult head is 154 mm, the face width (cheekbone to cheekbone) is 143 mm, the outer width between the eyes is 98 mm, and the inner width between the eyes is 35 mm. Therefore, the distance from inner part of the eye to the external part of the ear (we refer to this as Y_f) is on average 54 mm, and the distance from the outer part of the eye to the external part of the ear (we refer to this as X_f) is on average 22.5 mm. Other space constraints are given by the average diameter of the eyeball of an adult, which is around 30 mm and by the safety distance that we need to maintain between the EE and eyeball before insertion, which is at least 30 mm. Therefore, the length of the lever l_3 is designed to be 80 mm in length (PA and FG distance in Fig. 3a). The last distance to consider is the distance between the plane tangent to the lens of the eyeball and the plane tangent to the back of the head, which on average is 170 mm (we refer to this as Z_f). This distance needs to be adjusted by correctly installing the robot base on the patient bed or on a support attached to it. The movement range of the EE along the Z axis is designed to be 74 mm, which can effectively ensure that before and after surgery the EE can be moved at the safe distance of 30 mm from the eyeball, even in the case of large eyeballs (average is 23 mm as reported in [27]). At the same time, according to the working range of the robot's pitching motion, the length of l_4 should be larger than the thickness of l_2 and l_3 under critical conditions (Ψ at minimum or maximum values).

We now want to optimise the position of the linear actuator that controls the R motion at the EE. To do so we can adjust the position of point H on the AD rod which is not yet constrained. According to (7), by calculating the differential of Ψ with respect to Δl_d, the magnitude of the change in pitch angle corresponds in respect to the extension of the linear actuator can be obtained as follows:

$$\frac{d\Psi}{d\Delta l_d} = \frac{2\Delta l_d}{\sqrt{1 - (l_7^2 + l_{12}^2 - (l_{11} + \Delta l_d)^2)/(2l_7 \cdot l_{12})}} \tag{19}$$

The change of point H will cause the change of the virtual rod l_{12}. Theoretically, the length of rod l_{12} can vary in the range $(0, \sqrt{l_4^2 + l_9^2 + 2l_4 \cdot l_9 \cdot cos\,\alpha})$. When the value of l_{12} approaches 0, $d\Psi/d\Delta l_d$ will tend to be the largest. In this case, the motion efficiency is the highest. On one hand, a small displacement Δl_d produced by the linear actuator motor can produce a large pitch motion. On the other hand, this magnifies the influence of the motor motion error in the pitch motion, which seriously affects the motion accuracy of the EE. In addition, the stable triangular structure formed by the linear actuator motor and the rod AD and the rod CD will also become smaller, reducing the robot's motion stability. This can affect the long-term performance of the system in terms of precision.

As the value of l_{12} increases, these negative effects are reduced, but the efficiency of the motor drive will decrease. As the value of l_{12} approaches $\sqrt{l_4^2 + l_9^2 + 2l_4 \cdot l_9 \cdot cos\,\alpha}$ and the connection point H approaches joint A, the telescopic shaft of the linear push rod motor will interfere with the bottom rod of the robot. In the real system in fact is not possible to reach the theoretical maximum l_{12}. To find the best trade-off between pitching motion transfer efficiency, motion stability and robot motion accuracy, we need to determine the optimal position range of the connection point H, so the following optimisation is considered for l_{12}.

$$if \quad l_9 - (l_{int}/sin(\Psi_{min} - \alpha)) \le 0 \tag{20}$$

$$\begin{cases} (2-\tau)l \le l_{12} \le \left(1 - \dfrac{\Delta l_d}{l_{line} + l_{11}}\right)\left(l_4 + l_9 - \dfrac{l_{int}}{sin(\Psi_{min} - \alpha)}\right) \\ l = l_7\cos\Delta\Psi + \sqrt{l_7^2\cos^2\Delta\Psi - l_7^2 + (l_{11} + \Delta l_{line})^2} \end{cases} \tag{21}$$

Where l_{line} is the linear actuator motor range, l_{int} is the interference height between AB and CH, τ is the parameter determining the ratio between transmission accuracy, the transmission efficiency and structural stability that affects the structure, $\Delta\Psi$ is the pitch motion accuracy, Δl_{line} is the movement accuracy of the linear actuator motor.

According to the functional relationship between l_{12} and l_5, we can use the value range of l_5 to determine l_{12} using the following expression:

$$if \quad l_9 - (l_{int}/sin(\Psi_{min} - \alpha) > 0 \tag{22}$$

$$\begin{cases} (2-\tau)l \le l_4 + l_5 \le \left(1 - \dfrac{\Delta l_d}{l_{line} + l_{11}}\right)\left(l_4 + l_9 - \dfrac{l_{int}}{sin(\Psi_{min} - \alpha)}\right) \\ l = l_7\cos\Delta\Psi + \sqrt{l_7^2\cos^2\Delta\Psi - l_7^2 + (l_{11} + \Delta l_{line})^2} \end{cases} \tag{23}$$

$$sin\,\Psi_{min} = \frac{l_5 sin\,\alpha}{l_{12}} \cdot \frac{l_7^2 + l_{12}^2 - (l_{11} + \Delta l_{line})^2}{2l_7 l_{12}} \sqrt{\left(1 - \frac{l_5^2 sin^2\alpha}{l_{12}^2}\right)\left(1 - \frac{[l_7^2 + l_{12}^2 - (l_{11} + \Delta l_{line})^2]^2}{4l_7^2 \cdot l_{12}^2}\right)} \tag{24}$$

where l is one of the solutions of (23). Because the connection point H can be either above or below the joint G we need to distinguish these two scenarios for optimising l_{12}. According to the above design scheme, when we determine the value of τ and the value of l_4, we can obtain the optimal design range of l_{12}, which determines the optimal position of point H.

F. Prototype System Design and the EE Workspace

The proposed robot is 300 mm long, 50 mm wide and its height is 230 mm. The integrated system and all its components are presented in Fig. 4.

The parameters resulting from the calculation in the previous paragraph are presented in Table I. As discussed, the final system embeds 4 DOFs for the movement and orientation of the EE and 1 DOF to control the opening and closure of the forceps. We use a harmonic reducer to connect two Maxon DC brushed motors (MAH 20 and ECXSP08M, Maxon, Maxon Motor Ag, Switzerland) to drive the Φ DOF and the Θ DOF respectively. The motor labelled M1 in Fig. 4a is enclosed in cylindrical structure connected to robotic chain in four points. In this way, the error caused by the gaps in the gear transmission that could affect the accuracy of the deflection movement of the system can be eliminated.

A 1024-thread encoder is installed at the rear of the motor to reach an orientation accuracy of $0.0008°$ .We use a high-precision stepper motor to drive a ball screw (CPC corporation, Taiwan, China) that then drives the EE to achieve a linear motion of 5 μm per step on the R DOF. As mentioned above, the DC linear actuator motor (YINSHI LA50-022D/P, Beijing Yinshi Robotics Technology Co., Ltd., Beijing, China) installed on the diagonal of the parallelogram is used to drive the pitch motion of the entire double articulated parallelogram structure. Finally, based on the literature review conducted by the authors on research and commercial system, it is the first time in the field of eye microsurgical robots that opening and closure control of the surgical forceps at the EE is achieved. The remaining passive joints are connected by stepped shaft screws with bearings and gaskets. For the EE, we design a custom enclosure for a high-precision stepping drive motor and lead screw module to drive the opening and closing of a 25 Gauge (0.5 mm diameter) intraocular surgical forceps.

The actuation mechanism of the EE is presented in Fig. 4b. The external rod of the intraocular surgical forceps is fixed on the mechanical force sensitive rhombus mechanism under the rotating gear. The force sensitive structure (density: 1.3 g/cm³, Young's modulus: 2.5 GPa, Poisson ratio: 0.23, Resolution: 0.06 mN) can amplify the axial force on the surgical forceps and produce corresponding deformation in the embedded FBG sensor. As for the friction and lateral contact force between forceps and tissue, they can be measured using three FBGs glued on the forceps outer cylinder. The forceps outer cylinder is connected to the slider and the sliding bearing as shown in Fig. 4b. The movement of the slider drives the outer cylinder of the forceps to move back and forth axially along the forceps rod. The forceps closure is achieved by compressing the lower edge of the outer cylinder and deforming the two forceps flaps around the joint J. The sliding bearing moves along the guide rail to ensure stability of the opening and closing of the flaps. Most of the structural components of the surgical robot are custom made CNC (5 µm) metal elements made of aviation-grade aluminium alloy. the EE connector is 3D printed using biocompatible materials (10 µm) . The commercially available (Sihong Ophsurin Co., Ltd., Jiangsu, China) titanium-alloy forceps used for this system are widely used in clinics. They were integrated without the handle and manual opening mechanism they are usually sold with for clinical use. For simpler integration the robot embeds only the metal cylindrical hollow shaft that is translated to generate the opening and closure of the forceps flaps. Through both simulation and experimental validation on the prototype system, the workspace of the surgical forceps can be determined. This is compared with the eyeball volume aligning the RCM with the eyeball surface as shown in Fig. 5. We used as reference the anatomical parameters of the adult eyeball reported in [27] to simplify the eyeball into a sphere with a diameter of 23 mm. Through the analysis of the simulation results, we can get that the range of motion for Φ is 90°, going from -45° to 45° in respect to the axis passing by the RCM. Similarly, the range of Ψ is 55°, from 60° to 115°, and the range of Θ is 90°, from -45° to 45°. The maximum depth achievable along Z by the surgical forceps is 30 mm. The maximum opening and closing angle of the forceps flaps is $\gamma = 12°$. As a result, and as also clearly shown in Fig. 5, the workspace of the surgical forceps embedded in the proposed robot is larger than the posterior part of the eyeball, hence, each point on the surface of the retina can be reached.

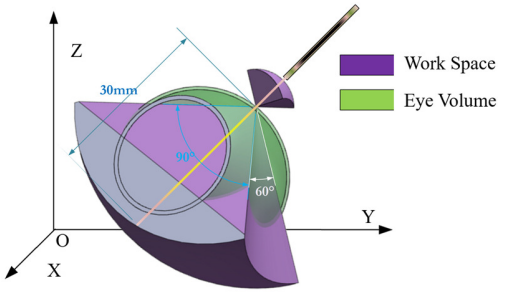

Figure 5 – Workspace of the EE and eyeball volume (section view).

Table I - OmSR Parameters

Parameter	Value	Unit
$l_1 = l_4 = l_8$	35	mm
$l_2 = l_3$	80	mm
l_5	13.5	mm
l_6	63.2	mm
$l_7 = l_{10}$	125	mm
l_9	75.7	mm
l_{11}	109.5	mm
Δ_d	35.5	mm
r	0.6	mm
α	27.6	°

III. Experimental Results and Discussion

Motion accuracy is the most important metric to evaluate the performance of the proposed system. Therefore, the motion accuracy of each moving joint, the motion accuracy of the surgical forceps on the EE and the stability of RCM point of the OmSR designed in this paper are experimentally measured.

A. *Measurement Method of End Motion Accuracy*

To assess the motion accuracy of the proposed system, we use Hall-effect and photoelectric encoders embedded in the motors to measure the joint movements. Proprietary software for each driver is used to display these data under a given input trajectory. Compared with the measurement of joint motion accuracy, it is much more difficult to measure the motion accuracy of the surgical forceps at the EE with traditional sensors, like the Hall-effect encoders used elsewhere. This is mainly due to the small diameter of the outer cylinder of the surgical forceps, to the even smaller scale of the flaps and to their small range of motion. Therefore, high-resolution imaging is used to detect the motion of the flaps rather than sensors embedded in the robotic structure. A high-speed camera (1080p, 50 Hz) is used to capture the motion of the surgical forceps. The recorded video is then used to create a sequence of images using two different sample times: 20 ms

and 50 ms. The coordinate value of the marking point (J point) at the end of the surgical forceps in the pixel coordinate system can be obtained using image segmentation on each frame analysed. At the focal distance considered in these experiments each pixel measured 6 µm. Finally, coordinate transformation and data processing are carried out to evaluate the trajectory of point P. The conversion between pixel and world coordinate system is shown in (25).

$$Z_C \begin{bmatrix} u \\ v \\ 1 \end{bmatrix} = \boldsymbol{K} \begin{bmatrix} R & t \\ 0^T & 1 \end{bmatrix} \begin{bmatrix} X_w \\ Y_w \\ Z_w \\ 1 \end{bmatrix} \tag{25}$$

Here, μ and v are the coordinates in the pixel coordinate system, and R and t are the rotation and translation matrix of the camera in the world coordinate system respectively, Z_C is the Z-axis in the camera coordinate system and X_w, Y_w, Z_w is the world coordinate system.

$$\boldsymbol{K} = \begin{bmatrix} \frac{1}{dx} & 0 & u_0 \\ 0 & \frac{1}{dy} & v_0 \\ 0 & 0 & 1 \end{bmatrix} \begin{bmatrix} f & 0 & 0 & 0 \\ 0 & f & 0 & 0 \\ 0 & 0 & 1 & 0 \end{bmatrix} \tag{26}$$

Here $\boldsymbol{K}$ is the camera intrinsic transformation matrix, which can be obtained through camera calibration, while dx and dy are the physical dimensions of a pixel along the X and Y directions in the image coordinate system and f is the focal length of the camera. To evaluate the performance of the system in terms of desired joint trajectory, measured joint trajectory and the EE position error for the 5 DOFs considered a sinusoidal signal is used as input signal for Motor 1 to 3, while a triangular and a trapezoidal position profile are used for Motor 4 and 5 respectively, to verify the motion error of the spin motion of the EE and the opening and closing.

The data collected during these experiments are presented in Fig. 6. Here the data of desired joint trajectories, measured joint trajectories and the EE position error for the five motors are presented separately and for motors 1, 2 and 3 also the joint output errors used to reflect the performance of the motor controller are plotted. The motion error of point P is also evaluated for rotational DOFs Ψ and Φ to evaluate the stability of the EE.

B. EE Motion Error

For the Φ DOF, the average error of joint output is 0.000394 ° and the repeated positioning error is 0.00703 °. For this DOF, the end motion error of surgical forceps is -17.6 µm with a standard deviation of 0.1075 µm. For the Ψ DOF, the average output error of linear push rod motor is -24 µm, and the repeated positioning error is -12.5 µm. For this DOF, the end motion error of surgical forceps is 28.8 µm and the standard deviation is 0.1094 µm. For the R linear motion, the average error of the joint output is 43 µm, and the repeated positioning error is 0.6 µm . For this DOF, the motion error of the end of the surgical forceps is -29.7 µm. Standard deviation is 0.0966 µm. The spin motion error of the EE is $-0.175°$, and the opening and closing motion error of the surgical forceps is 4.21 µm. The average motion error at the EE for each joint is less than 30 µm. By comparing it with every joint output error, we assume that most of the motion error of the EE is due to manufacturing imperfections of the system. Solutions considering 3D-printed multi-material flexure joints for a robot have been proposed to solve the mechanical play issue in [28]. In medicine, the accuracy of

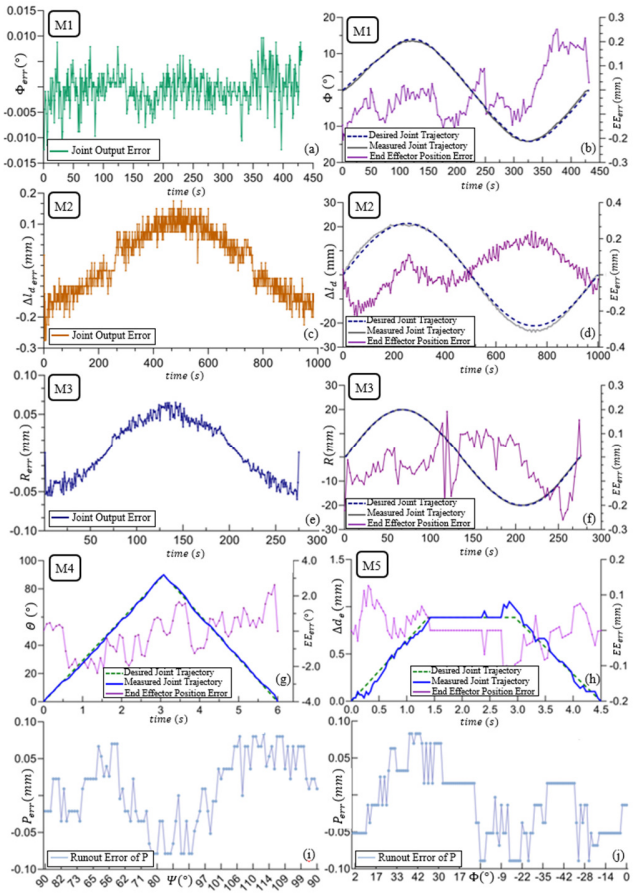

Figure 6 – Accuracy experiments for all the actuators in the kinematic chain of the proposed system and the EE positional error evaluation (a-h). Drifting error of point P for full range trajectory of DOFs Ψ and Φ. For actuator names refer to Fig. 4.

ophthalmic surgery is required to be less than 25 µm [29]. Therefore, more advanced control algorithms and error compensation algorithms are needed to further improve the robot accuracy in future developments.

Point P error has been analysed for the two most wide-range rotational degrees of the system. Through these experiments, we obtained that the average runout error of point P in the pitching motion is 8.4 µm and the maximum runout is 0.08 mm. The average runout error of deflection motion is -10 µm and the maximum runout is 0.083 mm, outperforming state-of-the-art systems like [30] and [2], the accuracy of which is about 5 mm and 1 mm respectively. Although the proposed system is yet to be validated in clinical settings, its performance in terms of RCM position accuracy and stability definitely meet the requirements of the envisioned application.

C. Tearing Experiment

To validate the system in a realistic scenario we also carried out an experiment simulating the hold and tear of the ILM. As phantom we selected the inner membrane of an eggshell with a wall thickness of 65-96 µm with an inner membrane of less than 20 µm of thickness. In this experiment, fertilized eggs were incubated for 12 ~ 13 days, part of the eggshell was removed, the inner shell and chorioallantois membrane was exposed, and a small amount of saline solution was used to simulate the physiological environment of the

retina inside the eyeball. This experiment is presented in Figure 4c. The surgical forceps successfully moved to the grasping point, grasped and peeled the shell and maintaining the micron-level precision in a predefined workspace of 4 cm^3. The experiment lasted 10 minutes in which the robot teared off a 1.32 cm^2 of membrane demonstrating the functionality of the system for the proposed task.

IV. Conclusion

In this work we proposed a novel double articulated parallelogram design to overcomes the limitations of state-of-the-art designs related to the misalignment between the sclera incision and then RCM. The novel integration of a high-precision surgical forceps in the EE will help clinicians to complete ophthalmic operations that cannot be completed by the existing surgical robotic systems, such as ILM tear, macular hole surgery, retinal detachment, and other fundus surgery. In addition the driving modules of the joints were optimised based on the results presented by the authors in [31].

Although the robot is designed for ILM and ERM removal, the robot can also be used for other anterior and posterior procedures by simply replacing the existing EE with the desired tool. The focus of this research was on the positional accuracy of the EE, hence, basic PID control (1 KHz frequency, closed loop control) have been used.

In future research, we intend to install the proposed system on a high-precision 3-DOFs cartesian platform, for robotic-assisted global positioning and calibration of this system. We will also focus on advanced control strategies and add OCT-microscope image guidance technology and haptic feedback through the FBG sensors glued on EE to the OmSR.

Acknowledgment

This research was funded in whole, or in part, by the Wellcome/EPSRC Centre for Interventional and Surgical Sciences (WEISS) [203145/Z/16/Z]; the Engineering and Physical Sciences Research Council (EPSRC) [EP/P027938/1, EP/R004080/1, EP/P012841/1]; the Royal Academy of Engineering Chair in Emerging Technologies Scheme [CiET1819/2/36]. For the purpose of open access, the authors have applied a CC BY public copyright licence to any author accepted manuscript version arising from this submission.

References

[1] W. H. Organization, "World report on vision," 2019.

[2] M. Zhou *et al.*, "Towards robotic-assisted subretinal injection: A hybrid parallel–serial robot system design and preliminary evaluation," *IEEE Trans. Ind. Electron.*, vol. 67, no. 8, pp. 6617–6628, 2019.

[3] J. Xiao, Q. Wu, D. Sun, C. He, and Y. Chen, "Classifications and Functions of Vitreoretinal Surgery Assisted Robots-A Review of the State of the Art," in *2019 International Conference on Intelligent Transportation, Big Data & Smart City (ICITBS)*, 2019, pp. 474–484.

[4] D. M. Silver and A. Csutak, "Human eye dimensions for pressure-volume relations," *Invest. Ophthalmol. Vis. Sci.*, vol. 51, no. 13, p. 5019, 2010.

[5] M. Spitznas, "Motorized teleguided stereotactic micromanipulator for vitreous microsurgery," *Arch. Ophthalmol.*, vol. 101, no. 4, pp. 623–630, 1983.

[6] C. N. Riviere, R. S. Rader, and P. K. Khosla, "Characteristics of hand motion of eye surgeons," in *Proceedings of the 19th Annual International Conference of the IEEE Engineering in Medicine and Biology Society.'Magnificent Milestones and Emerging Opportunities in Medical Engineering'(Cat. No. 97CH36136)*, 1997, vol. 4, pp. 1690–1693.

[7] B. Gonenc, E. Feldman, P. Gehlbach, J. Handa, R. H. Taylor, and I. Iordachita, "Towards robot-assisted vitreoretinal surgery: Force-sensing micro-forceps integrated with a handheld micromanipulator," in *2014 IEEE International Conference on Robotics and Automation (ICRA)*, 2014, pp. 1399–1404.

[8] A. J. Packer, *Manual of Retinal Surgery*. Butterworth-Heinemann Medical, 2001.

[9] W. E. Smiddy, W. Feuer, and G. Cordahi, "Internal limiting membrane peeling in macular hole surgery," *Ophthalmology*, vol. 108, no. 8, pp. 1471–1476, 2001.

[10] C. Haritoglou, C. A. Gass, M. Schaumberger, A. Gandorfer, M. W. Ulbig, and A. Kampik, "Long-term follow-up after macular hole surgery with internal limiting membrane peeling," *Am. J. Ophthalmol.*, vol. 134, no. 5, pp. 661–666, 2002.

[11] M. Morris and S. Tosunoglu, "Robotic Ocular Surgery," in *Florida Conference on Recent Advances in Robotics*, 2007, pp. 10–14.

[12] A. Guerrouad and P. Vidal, "SMOS: stereotaxical microtelemanipulator for ocular surgery," in *Images of the Twenty-First Century. Proceedings of the Annual International Engineering in Medicine and Biology Society,* 1989, pp. 879–880.

[13] J. Lussi *et al.*, "A Submillimeter Continuous Variable Stiffness Catheter for Compliance Control (Adv. Sci. 18/2021)," *Adv. Sci.*, vol. 8, no. 18, p. 2170118, 2021.

[14] B. Gonenc, J. Handa, P. Gehlbach, R. H. Taylor, and I. Iordachita, "A comparative study for robot assisted vitreoretinal surgery: micron vs. the steady-hand robot," in *2013 IEEE International Conference on Robotics and Automation*, 2013, pp. 4832–4837.

[15] J. T. Wilson *et al.*, "Intraocular robotic interventional surgical system (iriss): Mechanical design, evaluation, and master–slave manipulation," *Int. J. Med. Robot. Comput. Assist. Surg.*, vol. 14, no. 1, p. e1842, 2018.

[16] M. Nambi, P. S. Bernstein, and J. J. Abbott, "A compact retinal-surgery telemanipulator that uses disposable instruments," in *International Conference on Medical Image Computing and Computer-Assisted Intervention*, 2015, pp. 258–265.

[17] T. L. Edwards *et al.*, "First-in-human study of the safety and viability of intraocular robotic surgery," *Nat. Biomed. Eng.*, vol. 2, no. 9, pp. 649–656, 2018.

[18] A. Almony *et al.*, "Techniques, rationale, and outcomes of internal limiting membrane peeling," *Retina*, vol. 32, no. 5, pp. 877–891, 2012.

[19] A. Gijbels, N. Wouters, P. Stalmans, H. Van Brussel, D. Reynaerts, and E. Vander Poorten, "Design and realisation of a novel robotic manipulator for retinal surgery," in *2013 IEEE/RSJ International Conference on Intelligent Robots and Systems*, 2013, pp. 3598–3603.

[20] A. Gijbels, K. Willekens, L. Esteveny, P. Stalmans, D. Reynaerts, and E. B. Vander Poorten, "Towards a clinically applicable robotic assistance system for retinal vein cannulation," in *2016 6th IEEE International Conference on Biomedical Robotics and Biomechatronics (BioRob)*, 2016, pp. 284–291.

[21] K. Willekens *et al.*, "Robot-assisted retinal vein cannulation in an in vivo porcine retinal vein occlusion model," *Acta Ophthalmol.*, vol. 95, no. 3, pp. 270–275, 2017.

[22] J. Song, B. Gonenc, J. Guo, and I. Iordachita, "Intraocular snake integrated with the steady-hand eye robot for assisted retinal microsurgery," in *2017 IEEE International Conference on Robotics and Automation (ICRA)*, 2017, pp. 6724–6729.

[23] B. Gonenc, N. Patel, and I. Iordachita, "Evaluation of a force-sensing handheld robot for assisted retinal vein cannulation," in *2018 40th Annual International Conference of the IEEE Engineering in Medicine and Biology Society (EMBC)*, 2018, pp. 1–5.

[24] M. D. de Smet *et al.*, "Robotic assisted cannulation of occluded retinal veins," *PLoS One*, vol. 11, no. 9, p. e0162037, 2016.

[25] S. Nisar, T. Endo, and F. Matsuno, "Design and kinematic optimization of a two degrees-of-freedom planar remote center of motion mechanism for minimally invasive surgery manipulators," *J. Mech. Robot.*, vol. 9, no. 3, p. 31013, 2017.

[26] A. Poston, "Human engineering design data digest," *Washington, DC Dep. Def. Hum. Factors Eng. Tech. Advis. Gr.*, pp. 61–75, 2000.

[27] J. Wu, M. A. Nasseri, M. Eder, M. A. Gavaldon, C. P. Lohmann, and A. Knoll, "The 3D Eyeball FEA Model with Needle Rotation," *APCBEE Procedia*, vol. 7, pp. 4–10, 2013, doi: https://doi.org/10.1016/j.apcbee.2013.08.003.

[28] A. Pfeil, M. Siegfarth, F. Geiskopf, T. P. Pusch, L. Barbé, and P. Renaud, "Hydraulically-actuated compliant revolute joint for medical robotic systems based on multimaterial additive manufacturing," in *2019 International Conference on Robotics and Automation (ICRA)*, 2019, pp. 8401–8407.

[29] M. Zhou *et al.*, "Precision needle tip localization using optical coherence tomography images for subretinal injection," in *2018 IEEE International Conference on Robotics and Automation (ICRA)*, 2018, pp. 4033–4040.

[30] H. Su, A. Mariani, S. E. Ovur, A. Menciassi, G. Ferrigno, and E. De Momi, "Toward teaching by demonstration for robot-assisted minimally invasive surgery," *IEEE Trans. Autom. Sci. Eng.*, vol. 18, no. 2, pp. 484–494, 2021.

[31] N. Wang, X. Zhang, M. Li, H. Zhang, and X. Feng, "Improved Design and Dynamic Analysis of Ophthalmic Surgical Robot," in *2021 WRC Symposium on Advanced Robotics and Automation (WRC SARA)*, 2021, pp. 153–159.